













Lucy L’Ralph In-flight Calibration and Results at (152830) Dinkinesh

Amy A. Simon¹ , Hannah H. Kaplan¹ , Dennis C. Reuter¹, Matthew Montanaro², William M. Grundy³ , Allen W. Lunsford⁴, Gerald E. Weigle⁵, Richard P. Binzel⁶ , Joshua Emery⁷ , Jessica Sunshine⁸ , Carly Howett⁹, Harold F. Levison¹⁰ , Simone Marchi⁹ , Keith S. Noll¹ , and John Spencer⁹ 

¹NASA Goddard Space Flight Center, Solar System Exploration Division, Greenbelt, MD 20771, USA; amy.simon@nasa.gov

²Rochester Institute of Technology, Carlson Center for Imaging Science, Rochester, NY 14623, USA

³Lowell Observatory, Flagstaff, AZ 86001, USA

⁴American University, Physics Department, Washington, DC 20016, USA

⁵Big Head Endian, Winfield, KS 67156, USA

⁶Massachusetts Institute of Technology, Department of Earth, Atmospheric and Planetary Sciences, Cambridge, MA 02139, USA

⁷Northern Arizona University, Dept. of Astronomy and Planetary Science, Flagstaff, AZ 86011, USA

⁸University of Maryland, Department of Astronomy and Department of Geology, College Park, MD 20742, USA

⁹Planetary Science Institute, 1700 East Fort Lowell, Suite 106, Tucson, AZ 85719, USA and Atmospheric, Oceanic and Planetary Physics, University of Oxford, Clarendon Labs, Parks Road, Oxford, OX1 3PU, UK

¹⁰Southwest Research Institute, Boulder, CO 80302, USA

Received 2024 October 08; revised 2024 November 21; accepted 2024 November 27; published 2025 January 7

Abstract

The L’Ralph instrument is a key component of NASA’s Lucy mission, intended to provide spectral image data of multiple Jupiter Trojans. The instrument operates from ~ 0.35 to $4\ \mu\text{m}$ using two focal plane assemblies: a 350–950 nm multispectral imager, Multi-spectral Visible Imaging Camera (MVIC), and a 0.97– $4\ \mu\text{m}$ imaging spectrometer, Linear Etalon Imaging Spectral Array (LEISA). Instrument calibration was established through ground testing before launch and has been monitored during cruise utilizing internal calibration sources and stellar targets. In-flight data have shown that the instrument thermal performance is exceeding expectations, allowing for early updates to LEISA radiometric and pointing calibrations. MVIC radiometric performance remains stable more than 3 yr since launch. The serendipitous identification of a new flyby target, (152830) Dinkinesh, allowed testing of instrument performance and interleaved LEISA and MVIC acquisitions on an asteroid target. Both MVIC and LEISA obtained data of Dinkinesh and its moon, Selam, demonstrating that they show good spectral agreement with an S- or Sq-type asteroid, along with evidence of a $3\ \mu\text{m}$ absorption feature.

Unified Astronomy Thesaurus concepts: [Main belt asteroids \(2036\)](#); [Flux calibration \(544\)](#)

1. Introduction

Lucy is a NASA Discovery-class mission that launched in 2021 to investigate a previously unexplored class of bodies, the Jupiter Trojan asteroids. Lucy will fly past a number of these objects, visiting the Jupiter-leading L4 swarm in 2027 and the trailing L5 swarm in 2033 (H. F. Levison et al. 2021; C. B. Olkin et al. 2024). A major goal of the mission is to visit multiple Trojan asteroids with different spectral types to understand the compositional diversity of these bodies and their implications for solar system formation (C. B. Olkin et al. 2021). As these bodies are at 5 au and the flyby geometries vary, the Lucy instruments were designed to operate under low-illumination conditions with science requirements to observe effective surface brightness (intensity divided by incident solar flux, I/F) from as low as 0.0014 (visible) to 0.0019 (IR) to as high as 0.4 (both spectral regions; D. C. Reuter et al. 2023).

The Lucy L’Ralph instrument is two instruments in one: a multichannel visible to near-infrared (NIR) wavelength imager, and a shortwave IR imaging spectrometer (D. C. Reuter et al. 2023). It draws on heritage from the New Horizons Ralph and the OSIRIS-REx OVIRS instruments (D. C. Reuter et al. 2008; D. C. Reuter et al. 2018). The Multi-spectral Visible Imaging Camera (MVIC) uses time-delay integration (TDI) across six

separate 5024×64 pixel CCDs on a single substrate to construct images with spatial instantaneous field of view (iFOV) of $\sim 29\ \mu\text{rad pixel}^{-1}$. Filters over each CCD define the wavelength ranges of the six channels: the panchromatic (pan, Band 1: 350–950 nm), violet (Band 2: 375–480 nm), green (Band 3: 480–520 nm), orange (Band 4: 520–625 nm), phyllosilicate (Band 5: 625–750 nm), and NIR (Band 6: 750–950 nm). The Linear Etalon Imaging Spectral Array (LEISA) operates from 0.97 to $4.01\ \mu\text{m}$ using three linear variable filters (LVFs), with overlapping wavelengths, mounted above 1024×1472 pixels of a 2048×2048 HgCdTe infrared detector (H2RG), with an iFOV of $\sim 40\ \mu\text{rad pixel}^{-1}$ (D. C. Reuter et al. 2023). The LEISA effective wavelength varies with row down the array, as well as changing a small amount in the cross-track direction owing to filter smile (Figure 1).

The MVIC CCDs span a total of ~ 145 mrad in the cross-track and ~ 16 mrad in the TDI/along-track direction, with 0.9 mrad spacing between CCDs. The LEISA array spans ~ 41 mrad in the cross-track and ~ 60 mrad in the spectral/along-track direction (Figure 1). Both detectors share the same optical path, and an internal scan mirror is used to build up image cubes of the target (Figure 1) and can scan $\pm 4^\circ$ (± 70 mrad) on the sky in the along-track direction. Because LEISA uses an IR sensor, the focal plane assembly (FPA) must be passively cooled to reduce the background dark current (R. R. Blank et al. 2012); nominal LEISA FPA operating temperature is between 95 and 105 K, though it was calibrated

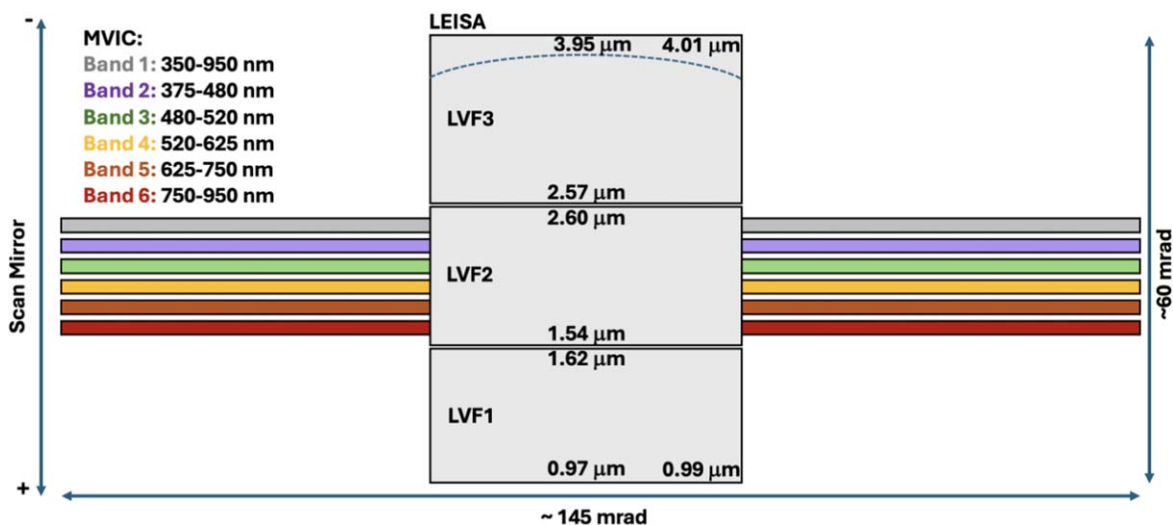


Figure 1. The L'Ralph focal planes to scale. LEISA and MVIC share the same optical path but have different fields of view and spatial resolutions. The instrument scan mirror is used to scan a target across the MVIC or LEISA filters to build up spectral image cubes.

over a range of 90–117 K. Nominal thermal conditions for the MVIC FPA are ~ 150 – 200 K, though it can operate at ambient temperatures. The instrument design and operation are described further in D. C. Reuter et al. (2023).

L'Ralph development followed a standard integration and test campaign that included performance verification tests to show that the instrument would achieve its science requirements. This campaign was composed of multiple smaller campaigns that included ambient testing for MVIC and thermal vacuum (TVac) cryogenic testing for both MVIC and LEISA. This paper describes the ground test campaigns and their limitations in Section 2. In Section 3 we discuss the in-flight calibration campaigns and their results. In Section 4 we demonstrate the performance verification conducted during the (152830) Dinkinesh flyby in 2023 November. Section 5 compares the Dinkinesh spectral data with those of other asteroids and ordinary chondrites. We conclude with upcoming calibrations in anticipation of the first Trojan asteroid flybys in 2027.

2. Ground Calibration Campaign

Instrument integration and testing occurred primarily in 2020 and was hampered by the global pandemic. As such, the testing was performed under very different conditions and restrictions than usual: testing teams were smaller, facilities were not operating at full capacity, finding or ordering needed equipment was challenging, and special care had to be taken to avoid illness while balancing constrained schedules (M. M. Garrison et al. 2022). To best optimize the testing time, experienced individuals were brought on from previous instrument calibration campaigns and the testing was planned in detail before execution. The calibration team utilized three 8 hr shifts, with overlap time, to minimize the downtime during testing.

For TVac testing, we utilized calibration ground support equipment (calGSE) that was developed for use on previous IR instruments and expanded for visible wavelength coverage for OSIRIS-REx OVIRS (M. M. Montanaro et al. 2014; A. A. Simon et al. 2018; A. A. Simon et al. 2021). This large, liquid-nitrogen-cooled system can be pushed into the TVac chamber with the instrument for radiometric, geometric, spectral, and pointing calibrations and is described in detail

in D. C. Reuter et al. (2023). TVac was split into two campaigns, each covering multiple thermal cycles, with vibration tests in between. One difficulty with L'Ralph testing is that while additional testing can be run for MVIC under ambient conditions, LEISA performance can only be checked under cryogenic temperatures.

The calGSE uses several sources to cover the full spectral range of L'Ralph. At short wavelengths, the calGSE uses a variable-attenuation, fiber-optic-fed, visible integrating sphere (VIS) coated with a Spectrafect lining (Labsphere 2017). Prior to use, the VIS was calibrated for single-fiber use at various attenuation levels and covering the spectral range from 250 to 2500 nm. The radiometric uncertainty was $\leq 1\%$ between 450 and 2300 nm. For infrared wavelengths, the calGSE includes a wide-aperture IR Flood source that can be operated at blackbody temperatures from 180 to 360 K. The IR source is National Institute of Standards and Technology (NIST) calibrated to better than 0.2%, confirmed prior to TVac (A. A. Pearlman et al. 2020). Additional sources were used to confirm pointing, pixel point-spread functions (PSFs), and spectral calibration (D. C. Reuter et al. 2023).

Despite the available calibration equipment, there were still challenges in replicating the deep space environment in the chamber, which led to several calibration uncertainties. First, the large amount of equipment in the chamber meant that, even with blankets and light shields, non-flight-like glints and reflections can cause apparent scattered light features. These scattered light features were especially problematic for MVIC, with its very wide field of view. Next, although the calGSE does include steerable small sources for pointing verification, L'Ralph includes an internal along-track scan mirror, and the instrument itself is mounted on a moving platform on the spacecraft, so a pointing vector must account for all three factors. Thermal effects added uncertainty to the TVac pointing vector measurements: the calGSE has a known pointing shift (in the L'Ralph along-track direction) from ambient metrology as it transitions to cryogenic temperatures (adds up to 2 mrad uncertainty), and we noted a thermal pointing shift internal to L'Ralph (up to 0.45 mrad over a 30 K change) as well. These uncertainties have a bigger effect on LEISA than MVIC because of the former's larger along-track field of view.

Lastly, LEISA is dependent on a combination of the VIS and the IR Flood sources for accurate radiometric calibration in the 2–3 μm range, where important spectral features occur, but also where the signal falls off rapidly from both calibration sources. Additionally, with a notional detector cutoff (50% response) of 3.95 μm , the LEISA detector has lower IR sensitivity when it is warm (e.g., R. R. Blank et al. 2012). At IR Flood source temperatures >270 K, the LEISA detector saturated at longest wavelengths, and when the detector was cold, it also showed evidence of out-of-band signal at these important wavelengths (infrared photons leaking into shorter-wavelength regions). This out-of-band signal is dependent on the source IR brightness and spectral shape, as well as the detector temperature-dependent response, and is common in these broad LVFs (A. A. Simon et al. 2021). However, out-of-band signal will not pose a problem for Lucy’s cold Main Belt and Trojan targets, as they will have few photons near 4 μm .

An additional calGSE issue was discovered during testing that mainly affected LEISA radiometric calibration. The electrical currents recorded from the VIS source during radiometric testing showed a discrepancy with pre-TVac calibration; these currents are used to convert the VIS output to known radiance levels and were above the values expected. After testing concluded, the chamber configuration was dismantled, and it was noted that the baffle on the critical variable-attenuation VIS fiber was out of alignment. During testing, this would result in some light exiting the VIS with fewer surface reflections and causing nonuniformity recorded as larger measured current values. This misalignment most affects calibration for wavelengths $\gtrsim 1100$ nm, where the Spectralect lining reflectance curves differ the most from the Spectralon baffle surface (LabSphere 2017). As the vendor calibration curves were based on an integrated power response across all wavelengths, we expected that an in-flight calibration correction would be needed, particularly to LEISA performance below ~ 2.6 μm .

3. In-flight Calibration

3.1. LEISA

LEISA was expected to be too warm for routine operations until after the spacecraft passes beyond 3 au from the Sun (D. C. Reuter et al. 2023). However, pointing the instrument radiator away from the spacecraft solar arrays does allow the focal plane to cool sufficiently to obtain usable signal, even above the maximum calibrated temperature (117 K). LEISA operation was first tested during the 2022 October Earth gravity assist. At 150 K, the detector was well above its nominal operational temperature, but valid spectral data were collected at some wavelengths (D. C. Reuter et al. 2023; J. R. Spencer et al. 2024). Subsequently, several tests and updated thermal models showed that LEISA could achieve its nominal operational temperatures at 2 au, if allowed to precool before science observations.

The ability to precool LEISA to operational levels was tested in 2023 July with a series of Arcturus stellar scans. In this campaign, the instrument pointing platform was off-pointed, allowing LEISA to cool to ~ 110 K, well within its nominal range. Using five separate cross-track positions on LEISA, the L’Ralph mirror scanned from dark space across the star and back to dark space, effectively moving Arcturus along the LEISA filters in the spectral direction from red to blue

wavelengths. Several things were noted in the scans: (1) the star did not cross the entire focal plane; (2) the star was scanned to move 1.5 pixels per integration, but the motion did not align with what was observed, with about a 2% difference; and (3) the calibration radiances for Arcturus were lower than reference values from 1.1 to 2.5 μm , as expected. Failure to scan the star across the entire focal plane (it stopped at about 1.1 μm , ~ 50 pixels from the detector end), would indicate either an offset in the pointing vector or that incorrect scan length parameters were used. However, the concurrent mismatch in star position and scan rate would mean that the scan mirror did not scan as commanded, or the pixel angular size was incorrect.

The LEISA stellar scans were repeated in 2024 March, offsetting the scan rate by 2% and the pointing by 1.6 mrad. In these new scans, the star tracked exactly 1 pixel per frame, confirming that the scan rate was now correct. However, the scan still stopped short of the end of the LEISA filters, by about 10 pixels, indicating that the scan length was incorrect. Fixed pointing checks were also run against the LORRI camera with fixed positions rather than scans to confirm relative pointing knowledge, as well as confirming the LEISA FWHM of the PSF as ~ 2 pixels. The combined tests proved that the pixel iFOV (and scan length) should be adjusted by 2%, from the TVac-derived rough angular size of 40 ± 3 $\mu\text{rad pixel}^{-1}$ to 40.75 ± 0.05 $\mu\text{rad pixel}^{-1}$. The LEISA pointing vector was also updated by 1.8 mrad relative to the internal scan mirror zero position.

For the radiance calibration, the flux from Arcturus was summed over 9×9 pixels for each wavelength, to account for the full extent of the PSF, as LEISA calibration was defined for extended sources. The summed values were converted to radiance using the TVac-derived calibration coefficients and then compared with a reference Arcturus spectrum (J. T. Rayner et al. 2009) convolved to the LEISA spectral resolution. The ratio of the measured to reference spectrum was found at each cross-track position that was scanned and interpolated across the entire LEISA field of view. The ratio of expected to measured radiance was ~ 1.01 at 1.1 μm , to a maximum of ~ 1.8 near 2.1–2.2 μm (Figure 2). The in-flight calibration below ~ 1.0 μm is not yet verified, as we do not have LEISA stellar data at these wavelengths.

A last effect to note for LEISA is optical fringing. During TVAC testing, some observations showed evidence of a repeating brightness variation, particularly at low light levels. This effect is seen in the Arcturus stellar scans, as well as in internal calibration source data (Figure 3). Although antireflective coatings are applied to all surfaces, optical modeling shows that the likely cause is a reflection off the detector to the back of the filters and back to the detector. The effect can be mitigated by creating fringe flats that can be applied after the data are calibrated.

Currently, fringe flats are created using the data themselves for each observation. For the internal sources (Figure 3), the full frame was already illuminated, but for a smaller object, such as an asteroid, a master frame was constructed that sums together the source illumination as it moved across the field of view (in effect, a “smeared” flat). Single-pixel artifacts were removed, and 2D median filters were applied to smooth the data in each filter. Next, a sliding Gaussian was iteratively fit, row by row and across each filter, and a local mean background level was calculated across multiple fringes. The resulting fringe flat was constructed by dividing the Gaussian model at

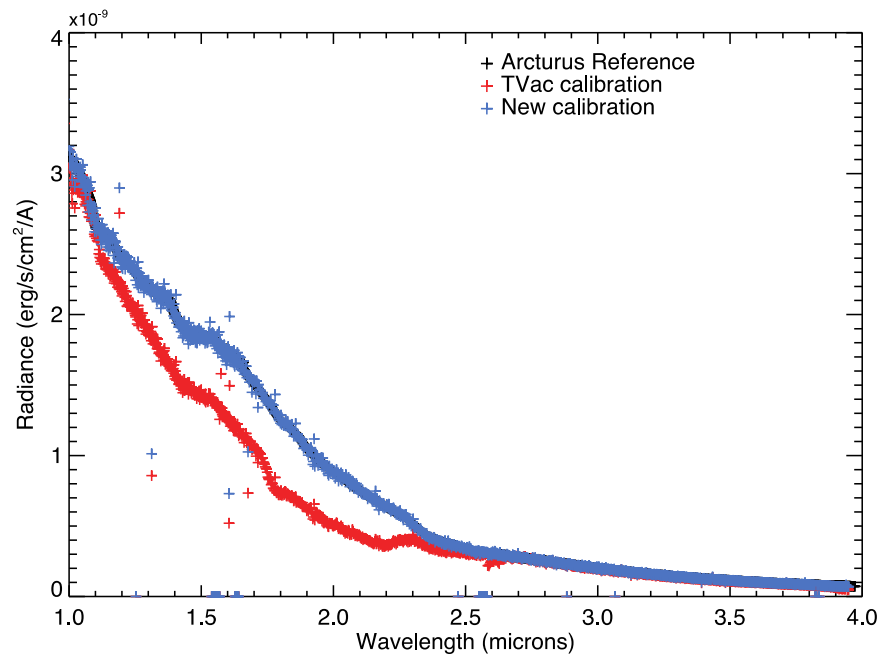


Figure 2. LEISA Arcturus calibration. The LEISA stellar scans were used to compare calibrated radiance with an Arcturus reference spectrum; the calibration coefficients from TVac (red points) were adjusted (blue points) to match the known radiance.

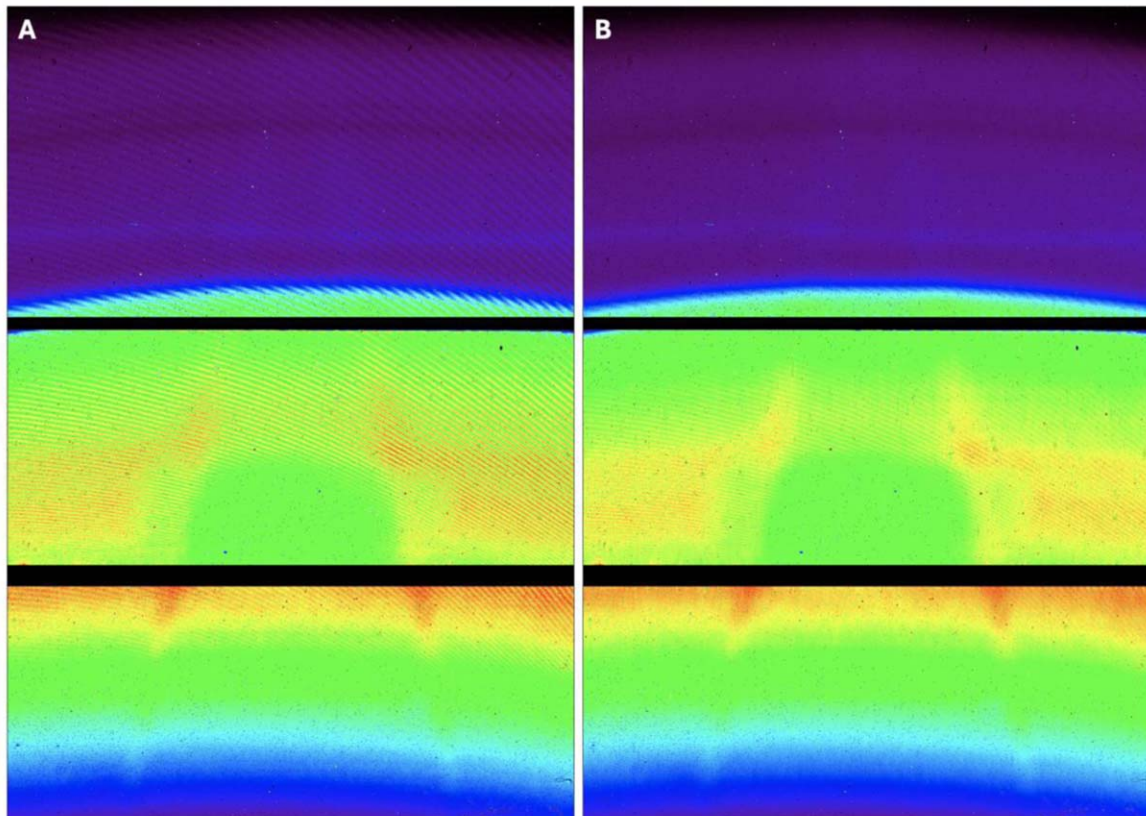


Figure 3. LEISA optical fringes in calibration data. For both frames, the long-wavelength end is at the top and the short-wavelength end is at the bottom. The round feature near the center is caused by the calibrator scatter plate, and the inverted-V-shaped feature across the bottom filters is from reflections off the cold snout surrounding LEISA. (a) Internal filament calibrator data show significant optical fringing apparent as higher-frequency diagonal lines. (b) Fringing is greatly reduced after applying a fringe flat correction.

each fringe by the local mean background. Attempts are underway to determine whether the fringe pattern can be more accurately modeled from optical properties for better removal,

but the current method does significantly reduce the fringes from up to 20% of the brightness value to a few percent or better. These team-derived Dinkinesh flats and their

documentation were delivered with the calibrated data to the Planetary Data System (PDS) for post-calibration processing by end users (D. D. Reuter et al. 2024a).

3.2. MVIC

MVIC operates at higher temperatures than LEISA, which has allowed for more extensive in-flight calibration while the spacecraft is in the inner solar system. Calibration data were taken of Earth and the Moon during Lucy’s first Earth gravity assist (EGA-1), each acquired at five cross-track positions. Other routine calibrations were completed on multiple occasions: 2022 May (0.97 au), 2023 March (1.74 au), and 2024 March (2.02 au). At each opportunity, radiometric stability was checked with an internal filament source, a solar calibration, and observations of three different star clusters, M6 (Butterfly Cluster, NGC 6405), M7 (NGC 6475), and the Wishing Well (NGC 3532). M6/M7 and the Wishing Well are each scanned at five cross-track positions to assess variation across the detector; pointing is repeated between each calibration opportunity, leading to comparable image sets from each of our routine calibrations.

Early analysis demonstrated that MVIC performance conforms with expectations from TVac testing and meets or exceeds mission requirements. The PSF does not vary across the detector and, with an FWHM of ~ 1.7 pixels ($50 \mu\text{rad}$), is consistent with requirements (D. C. Reuter et al. 2023). Lunar data from EGA-1 show good agreement with RObotic Lunar Observatory (ROLO) standard modeled data and with Moon Mineralogy Mapper hyperspectral images over the same lunar surface regions (D. C. Reuter et al. 2023), demonstrating that the radiometric calibration coefficients derived from TVac data are accurately calibrating data in all bands from counts to radiance. We were also able to show that the signal from scattering is $\ll 1\%$ for the angular range of observations pertinent to the Trojan encounters using the saturated EGA-1 Earth observations (D. C. Reuter et al. 2023).

Since the initial in-flight calibration results reported in D. C. Reuter et al. (2023), we have continued performance trending. The MVIC FPA temperature was 212 K in 2022 May, 156 K in 2023 March, and 160 K in 2024 March; we use TVac data taken at 152 K for comparison. Internal filament calibration data taken at similar temperature (TVac, 2023 March, 2024 March) shows better agreement than for the early higher-temperature data (2022 May), which are offset from the rest, as the instrument electronics and focal planes have not yet reached nominal flight temperatures. Fractional bias is $\pm 2\%$ for each of 5024 pixels across the detector in panchromatic, orange, phyllo, and NIR channels. The shortest visible channels, violet and green, have much higher fractional bias because they have very low signal (< 100 counts over background), but otherwise they show the expected agreement.

For the stellar calibrations, we used astrometry to find the celestial coordinates of each image to co-register images from the three calibration opportunities (2022 May, 2023 March, 2024 March). We then identified 400 stars that can be found in all three observations. Data are converted to calibrated radiance using calibration coefficients that were derived from TVac and tested on the Moon EGA-1 data. We find the center pixel for each star and sum over a 5×5 pixel area to account for the full extent of the PSF. When data from all three calibration opportunities are compared, there is $\pm 5\%$ agreement in radiance for the same star at similar positions across data sets

(Figure 4). As with the internal calibration data, agreement is best between the 2023 and 2024 March data sets taken at similar MVIC and electronics temperatures. Although MVIC was intended for extended rather than point sources, these stellar calibrations place an upper limit on radiometric uncertainty. When stars are tracked at multiple positions across the detector, radiance values are also $\pm 5\%$, indicating consistent calibration across the detectors.

4. Dinkinesh Flyby

On 2023 November 1, Lucy encountered Main Belt asteroid (MBA; 152830) Dinkinesh, which was added to the mission to provide an earlier opportunity to test flyby target tracking and science operations (H. F. Levison et al. 2024). Although the encounter occurred at 2.26 au, it was again hoped that LEISA could be precooled to allow for unsaturated data. Due to flyby constraints on pointing and timing, optimal LEISA precooling was limited, but the FPA cooled to 119 K, just above the calibrated operating range. The two focal planes cannot be commanded at the same time and require different scan parameters, so this flyby also tested the ability to interleave LEISA and MVIC observations (D. D. Reuter et al. 2024a; 2024b). For each focal plane, three scans were conducted around closest approach (C/A) with varying range and phase angles (Table 1).

As the Lucy system tracking performance was not yet characterized, the scans were padded for significant uncertainty in pointing positions. Both LEISA and MVIC conducted three target scans and used short exposure times, as Dinkinesh is more reflective and closer to the Sun than the Trojan targets for which the instrument is optimized. For the LEISA scans, the exact pointing and scan rate were still in question at the time of Dinkinesh planning. To adjust for the limited knowledge and to keep the scan length reasonable, we scanned at a rate equivalent to ~ 1.55 (assuming $40 \mu\text{rad pixel}^{-1}$) pixels per frame with integration times of 70–80 ms per frame; see Table 1. This scan rate accounted for the 2% pixel size/scan rate issue identified in the 2023 July stellar calibrations, while keeping Dinkinesh within the extended PSF of a pixel. Dinkinesh’s satellite, Selam, was unknown at the time of planning (H. F. Levison et al. 2024), but other flyby aspects, such as changing phase angle and range during observations, were included in the planning process.

While MVIC can only be scanned across the object in the TDI (positive scan) direction, LEISA can be scanned in either direction. The first LEISA observation was conducted scanning from short to long wavelengths, while the other two scanned from long to short wavelengths. The scan direction primarily matters during the period of rapidly changing phase angles near C/A, when the shorter wavelengths may saturate but the longer wavelengths can benefit from increased illumination at lower phase angles (see Table 1 and Figure 5). Figure 5 also shows an individual frame from the LEISA C/A scan, as well as the panchromatic (Band 1) C/A image from MVIC.

During the flyby, MVIC collected data with its shortest possible integration time (7.2 ms per TDI line). Because of the pointing margin, the MVIC data sets cover ~ 1500 pixels in the along-track direction even though Dinkinesh only spans ~ 50 MVIC pixels at C/A. Dinkinesh and Selam are well exposed in all channels and images except for a small number of saturated pixels in the C/A image panchromatic channel. Calibrated radiance was converted to I/F by dividing by the CALSPEC

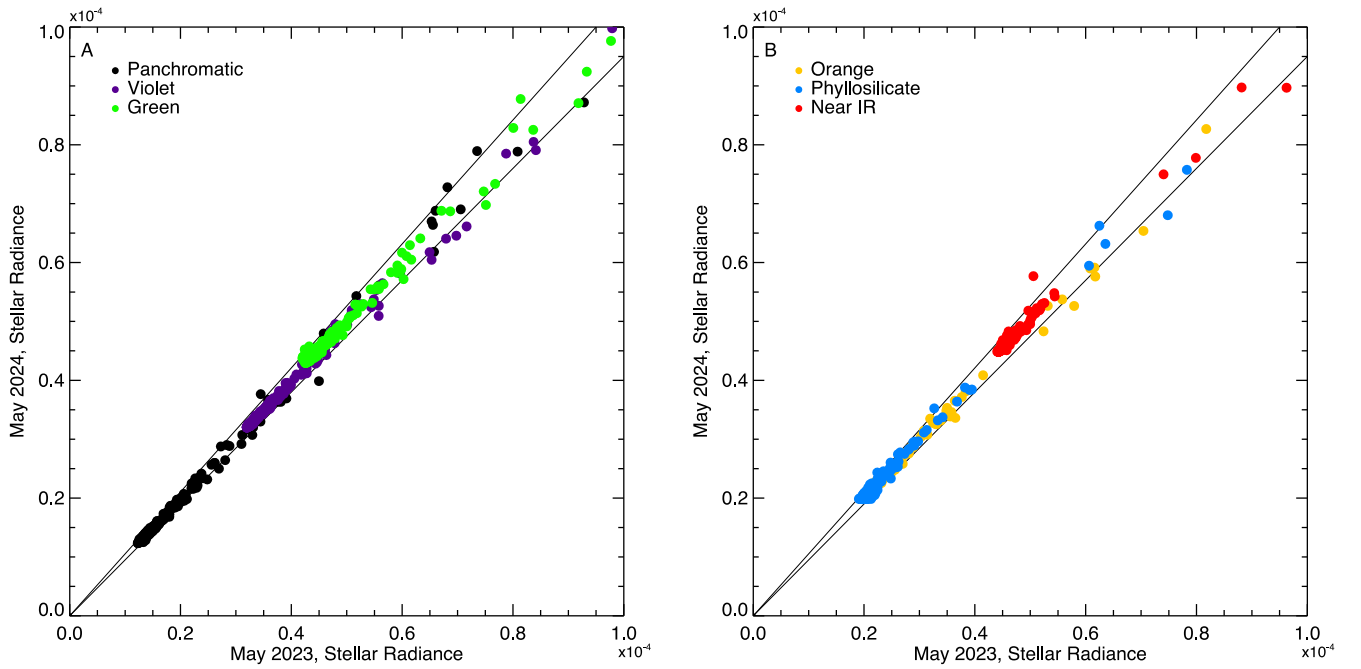


Figure 4. MVIC stellar calibrations from 2023 March and 2024 March. (a) Panchromatic, violet, and green channels; (b) orange, phyllosilicate, and NIR channels. Stars were chosen separately for each channel based on signal level, and all bands show stable radiometric performance $\pm 5\%$ over that time period.

Table 1
L’Ralph Dinkinesh Observations

Time	Scan	Phase Angle Start (deg)	Phase Angle End (deg)	Range Start (km)	Range End (km)	Frame Rate (ms)	MVIC TDI per Band
-368 s	MVIC approach		104		1700	7.2	4, 8, 8, 8, 8, 8
-289 s	LEISA approach	101	90	1372	897	80	
-55 s	MVIC C/A	60	58	485		7.2	4, 4, 4, 4, 4, 8
+92 s	LEISA C/A	16	31	614	860	70	
+250 s	MVIC departure		40		1215	7.2	4, 4, 4, 4, 4, 8
+337 s	LEISA departure	46	49	1675	2033	75	

solar flux (R. C. Bohlin et al. 2014) integrated over the MVIC bandpasses and scaled to Dinkinesh’s solar distance (Figure 6(a)). There is a 96-pixel offset between each MVIC channel in a scan (64 pixels per detector plus 32-pixel space between detectors). Each channel is shifted by the appropriate offset to align the six bands so that spatially related pixels are aligned; limb data do not match exactly owing to the changing viewing conditions and target size within the data set.

Using disk-averaged spectra from the three MVIC scans, we calculate a phase curve and find $\sim 0.029 \text{ mag deg}^{-1}$ change related to phase angle. Because of the fast scan rate and the timing of the images, MVIC does not see significant phase change within a data set; there is a 2° phase change between the leading channel (pan) and trailing channel (NIR) in the C/A image and a $< 1^\circ$ change in the Approach and Departure images (Table 1). The phase curve for each band is assessed individually, and there is $\sim 0.009 \text{ mag deg}^{-1}$ difference between the reddest and bluest portions of the MVIC spectrum. As Dinkinesh and Selam spanned only a small number of illuminated pixels, we focused on analyzing the C/A and Departure scans to generate spectra for comparisons. We used the average $0.029 \text{ mag deg}^{-1}$ change to correct all spectra to a 30° viewing geometry (Figure 6(b)).

LEISA spectrum construction is a bit more complex. As each LEISA along-track pixel is a different wavelength, spectrum

generation requires tracking a surface area across each frame of the scan. To simplify this process, image cubes can be constructed for Dinkinesh and Selam from each scan by taking each column of each LEISA frame, corresponding to a distinct wavelength, and reprojecting it to the corresponding wavelength layer of an output cube. For our analysis, the reprojection was to the apparent sky plane at the time of each frame and centered on the target, accounting for target size changes during the scan. We did not account for the changing subspacescraft longitude and latitude on the target, nor were the data projected onto a shape model, limiting our ability to look for spectral variations on Dinkinesh’s surface. Additionally, we did not model or remove any thermal tail from the data, as the Dinkinesh radiances show no evidence of thermal emission. This is not surprising, since at 2.3 au the LEISA signal is dominated by reflected solar radiation for objects colder than $\sim 250 \text{ K}$, even at low I/F , and all of our spectra are disk averaged, including regions much cooler than the subsolar point.

The LEISA data were converted to I/F using the CALSPEC solar flux (R. C. Bohlin et al. 2014) convolved over the LEISA bandpasses and scaled to 2.26 au. The LEISA spectra were then generated by averaging over the illuminated pixels at each wavelength in each cube and then removing outliers two standard deviations from the mean and along filter boundaries

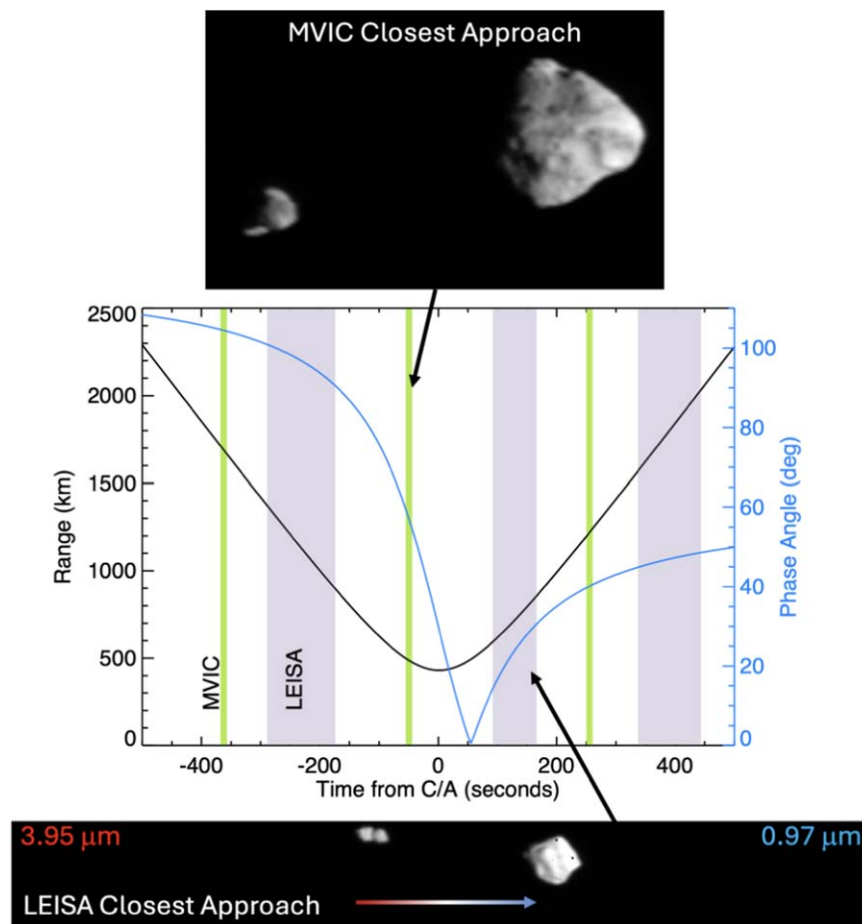


Figure 5. Dinkinesh closest approach views from MVIC and LEISA. The top panel shows the MVIC pan band image showing Dinkinesh (right) and Selam (left), while the bottom panel shows a single frame acquired near the center of the LEISA scan. The middle panel shows the changing range and phase angles during each of the LEISA and MVIC observations.

(Figure 6(c)). We applied conservative $\pm 7\%$ error bars on the I/F , from the rms of 5% uncertainty from the LEISA radiance and an assumed 5% uncertainty from the solar flux. Selam and Dinkinesh are spectrally similar, as expected if they share a similar origin (H. F. Levison et al. 2024). However, the brightness of the two bodies cannot be directly compared, as phase angle changed throughout the observations, particularly at C/A; that is, Selam crossed the same spectral element at higher phase angles than Dinkinesh, and in some scans it did not cross all wavelengths.

The LEISA Departure scan occurred when Dinkinesh was at a higher phase angle than the C/A scan (Table 1), but it did not change as significantly throughout the observation, only $\sim 3^\circ$. To determine the Dinkinesh NIR phase curve, we found the value that resulted in the best match between the two Dinkinesh scans when corrected to the phase angle at end of the C/A scan ($\sim 30^\circ$). This resulted in a best-fit photometric phase correction of $0.0316 \text{ mag deg}^{-1}$ with a $\chi^2 = 0.41$, ignoring any possible phase reddening or other surface parameters. A best-fit phase reddening was found by comparing the phase angle of the two scans and spectral slope between 1.1 and $3.7 \mu\text{m}$. With so many parameters simultaneously changing during the scans and the reduced long-wavelength sensitivity, the uncertainties are large, but we find a best-fit phase reddening I/F slope change of $\sim 0.0002 \mu\text{m}^{-1} \text{ deg}^{-1}$ (Figure 6(d)). No other surface parameters (i.e., roughness) could be reliably fit owing to the

changing object geometry and illumination in these limited scans.

5. Discussion

Visible and NIR spectra of the Dinkinesh system from the Keck and Gemini observatories show a red (i.e., positively increasing) spectrum from 0.45 to $0.8 \mu\text{m}$ and an absorption band centered near $1 \mu\text{m}$ (B. T. Bolin et al. 2023). These observations predicted that Dinkinesh is an S- or Sq-type asteroid. The phase-corrected, disk-averaged, MVIC spectra show increasing reflectance with wavelength that flattens in the NIR channel (Figure 6(b)). The NIR filter subtends part of the $1 \mu\text{m}$ absorption feature typical of S-type asteroids as indicated by the spectral flattening, but the effective wavelength of NIR is $\sim 0.75 \mu\text{m}$, which is too short to show a more significant downturn from a $1 \mu\text{m}$ absorption feature.

We also performed an initial analysis of spatial color variation on Dinkinesh using all channels in the MVIC C/A image that had a spatial resolution of $\sim 14 \text{ m pixel}^{-1}$. Given Dinkinesh's small size in our scans, MVIC would be more likely to show spatial variation than LEISA, which had a best spatial resolution of $\sim 25\text{--}35 \text{ m pixel}^{-1}$ near C/A. To first order, there is little variation in any channel or channel ratio across the surface. However, neither the LEISA nor MVIC image cubes have been registered to a shape model, and therefore an individual pixel's ground location and phase angle

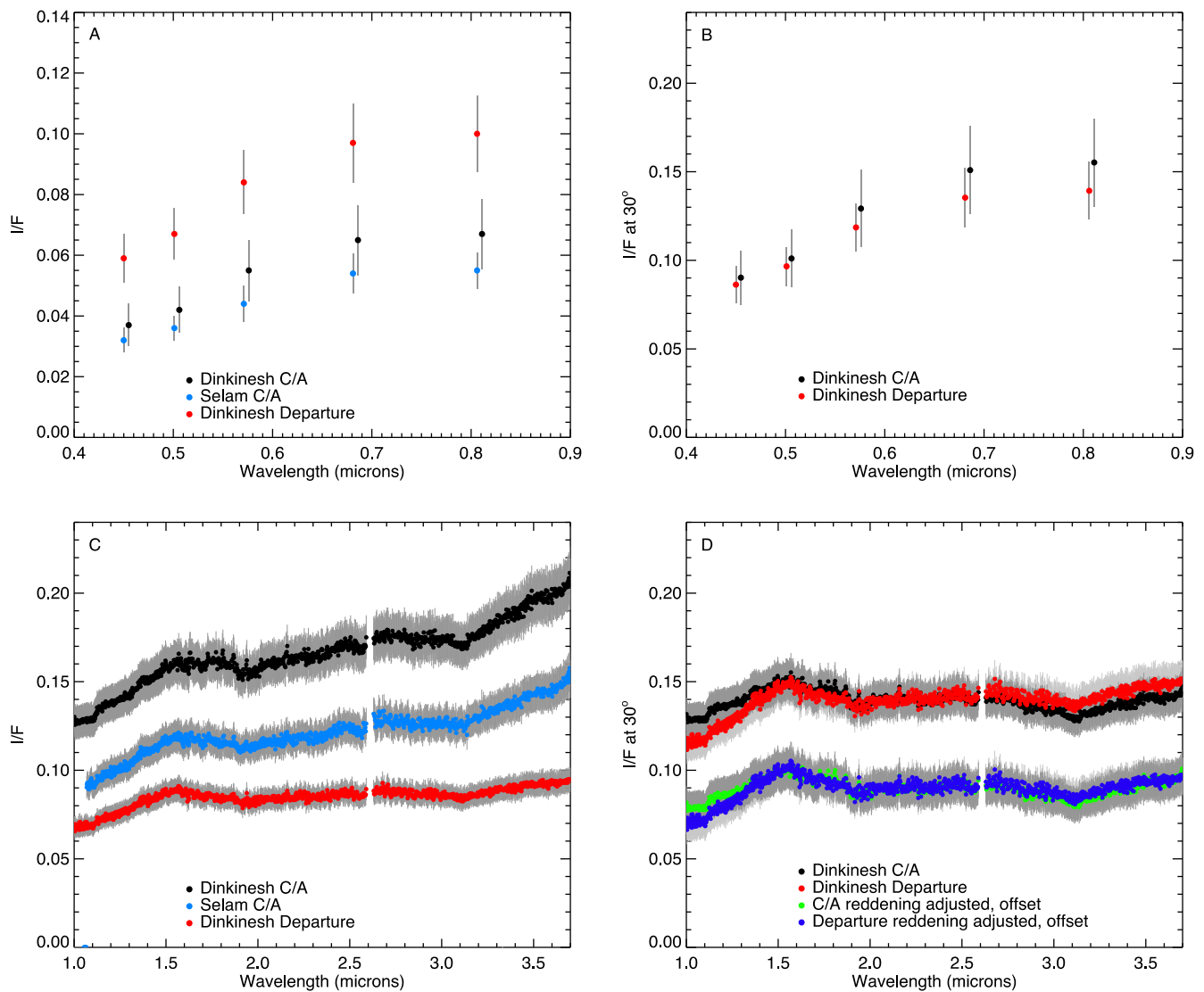


Figure 6. Spectra of Dinkinesh and Selam. (a) MVIC I/F for Dinkinesh closest approach (red) and at lower phase on departure (black). Selam is shown at closest approach and has a similar spectral shape to Dinkinesh (blue). (b) Simultaneously fit MVIC I/F scans phase corrected to 30° . (c) LEISA Dinkinesh spectrum from closest approach (black) and at higher phase on departure (red). Selam at closest approach again shows a nearly identical spectral shape to Dinkinesh. (d) Simultaneously fit LEISA scans phase corrected to 30° and with a phase reddening correction.

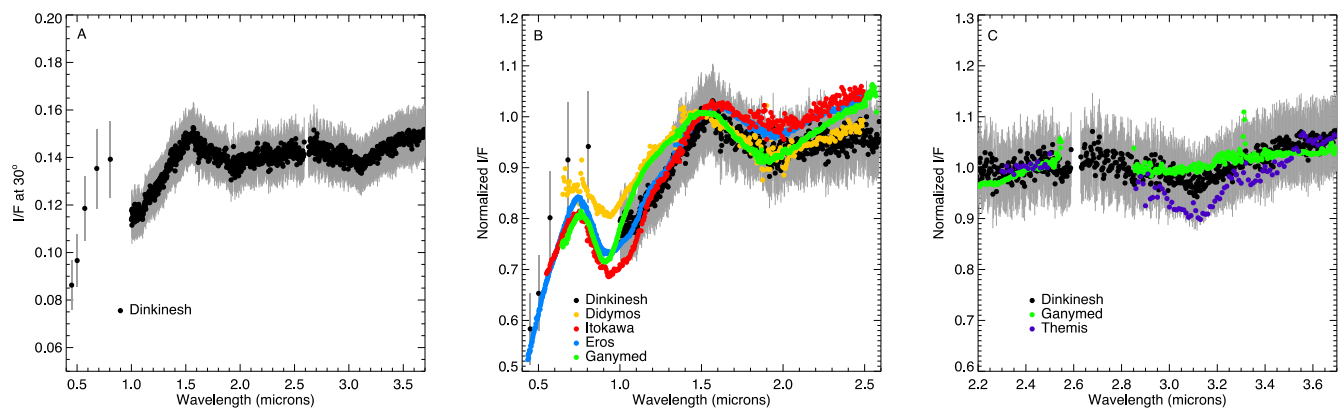


Figure 7. Dinkinesh spectral comparisons. (a) The composite MVIC and LEISA departure scan Dinkinesh data corrected to 30° phase. (b) The short-wavelength spectrum, normalized at $1.5 \mu\text{m}$, with comparisons to other S- and Sq-type asteroid spectra (R. P. Binzel et al. 2001, 2004, L. E. McGraw et al. 2022, D. D. Polishook et al. 2023). (c) Dinkinesh's $3 \mu\text{m}$ absorption band, normalized at $2.9 \mu\text{m}$, compared with that of Ganymed and Themis (A. Rivkin & J. Emery 2010, L. E. McGraw et al. 2022).

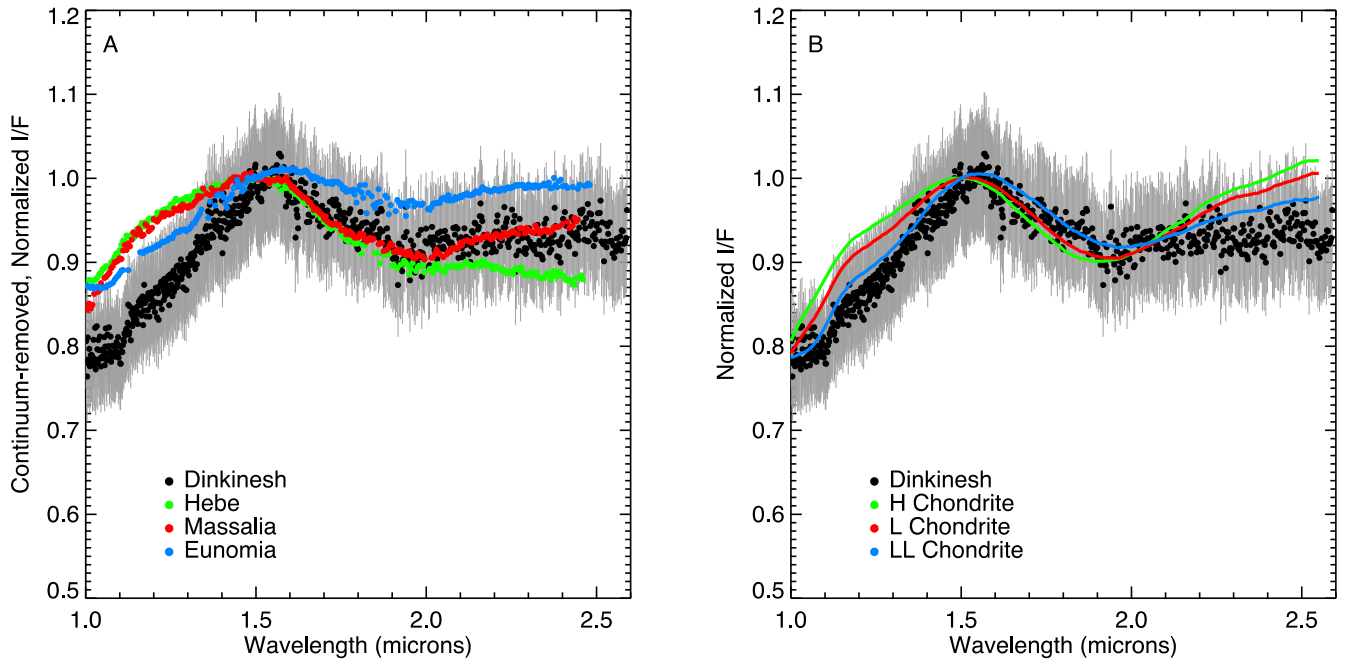


Figure 8. Comparison of Dinkinesh with representative asteroids and their corresponding chondrites. (a) Dinkinesh’s spectrum (black points), continuum-removed and normalized at $1.5 \mu\text{m}$, compared with those of Hebe, Massalia, and Eunomia (R. P. Binzel et al. 2019). (b) The same comparison, but with average ordinary chondrite subtype spectra (T. L. Dunn et al. 2010).

may not be accurate across bands or spectral channels. Instead, we focus on full-disk spectral comparisons with other S-complex asteroids.

To better compare the spectral type of Dinkinesh, we combined the MVIC and LEISA data to obtain a complete spectrum from 0.4 to $3.7 \mu\text{m}$. For each focal plane, the Departure scan data were corrected to 30° phase with their respective phase curves (Figure 7(a)), as these data had fewer uncertainties from varying phase angle during the LEISA scan. The Dinkinesh spectrum has a clear $2 \mu\text{m}$ absorption band, the suggestion of the $1 \mu\text{m}$ band (Figure 7(b)), and a possible absorption near $3 \mu\text{m}$ (Figure 7(c)). From 0.4 to $2.5 \mu\text{m}$, Dinkinesh’s spectrum shows a reasonable spectral shape for an S-complex asteroid, for example, (433) Eros, (25143) Itokawa, (65803) Didymos, and (1036) Ganymed (R. P. Binzel et al. 2001, 2004; L. E. McGraw et al. 2022; D. D. Polishook et al. 2023). Note that the Dinkinesh $1 \mu\text{m}$ band depth is highly uncertain, as the LEISA calibration near these wavelengths needs to be repeated, as discussed in Section 3.1.

The S-complex asteroids’ 1 and $2 \mu\text{m}$ absorption bands are due to pyroxene and are common in stony meteorites; S-complex subtypes are distinguished by the varying depth and central wavelength of the 1 and $2 \mu\text{m}$ absorption bands, as well as spectral slopes. (Figure 7(b)). Dinkinesh’s $2 \mu\text{m}$ band is centered near $1.95 \mu\text{m}$ with a depth of $\sim 6\%$ and an FWHM of $\sim 0.45 \mu\text{m}$. Unfortunately, the parameters of the $2 \mu\text{m}$ band alone cannot generally be used to assess the pyroxene chemistry or determine analog asteroid or meteorite subtypes. We therefore turned to direct spectral comparisons (i.e., curve matching) between the LEISA spectra of Dinkinesh and published spectra of ordinary chondrite meteorites (T. L. Dunn et al. 2010) and S-complex near-Earth asteroids (NEAs) and MBAs (L. E. McGraw et al. 2022; M. M. McAdam et al. 2024).

Curves were compared after dividing out a spectral slope, computed as the best-fit line of each spectrum from 1.2 to

Table 2
Dinkinesh Wavelength Fits for the $1.5 \mu\text{m}$ Peak and the $2 \mu\text{m}$ Absorption

	$1.5 \mu\text{m}$ Peak Center (μm)	$2 \mu\text{m}$ Band Center (μm)
Close approach	1.51 ± 0.02	1.95 ± 0.02
Departure	1.52 ± 0.02	1.94 ± 0.06

$2.45 \mu\text{m}$. Although S-complex asteroids show a continuum of 1 and $2 \mu\text{m}$ band centers, several provide good matches to L, LL, and H chondrite meteorites, for example, (6) Hebe (H), (20) Massalia (L), and (15) Eunomia (LL) (R. P. Binzel et al. 2019; M. M. Marsset et al. 2024). The MIT-Hawaii Near-Earth Object Spectroscopic Survey (MITHNEOS) spectra of these asteroids compare well with Dinkinesh’s $2 \mu\text{m}$ band, particularly for Massalia and Eunomia (R. P. Binzel et al. 2019; Figure 8(a)). In the meteorite collection, the average LL and L chondrite meteorites provide better matches to Dinkinesh than H chondrites (Figure 8(b)). The poorer fits of the H chondrites are mostly due to the peak near $1.5 \mu\text{m}$ (i.e., between the two absorption bands) being at a shorter wavelength than in the other ordinary chondrites. The H chondrite $2 \mu\text{m}$ band center also tends to be at a shorter wavelength than in Dinkinesh.

We also computed the location of the $\sim 1.5 \mu\text{m}$ peak and $2 \mu\text{m}$ band center in the spectra of the meteorites and Dinkinesh (Table 2 and Figure 9). The ordinary chondrite meteorites cluster by subtype in the parameter space of $1.5 \mu\text{m}$ peak center versus $2 \mu\text{m}$ band center similarly to how they cluster in $1 \mu\text{m}$ band center versus $2 \mu\text{m}$ band center (T. L. Dunn et al. 2010). The similar clustering makes sense, in that the location of the $1.5 \mu\text{m}$ peak is set by the locations of the two absorption bands that bound it, so it is heavily influenced by the $1 \mu\text{m}$ band. As such, even though we are not able to directly measure the $1 \mu\text{m}$ band center in the Dinkinesh spectra, we can use the $1.5 \mu\text{m}$ peak as a proxy in terms of meteorite comparisons. The

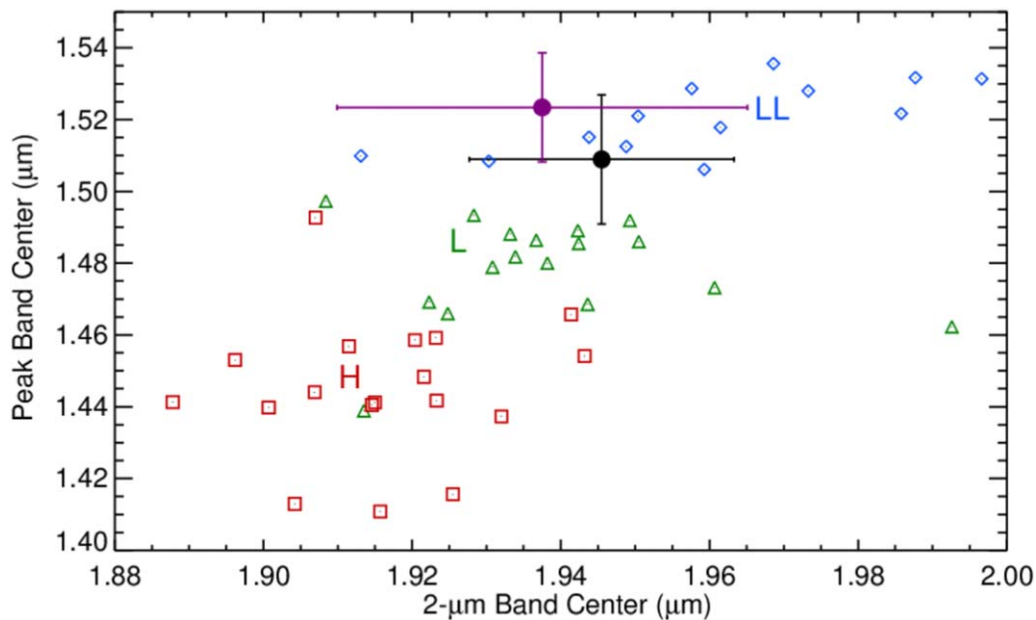


Figure 9. Locations of the centers of the $1.5\ \mu\text{m}$ peak and $2\ \mu\text{m}$ absorption in LL (blue diamonds), L (green triangles), and H (red squares) ordinary chondrites. These ordinary chondrite subtypes are distinguishable in this parameter space. The measured parameters for the Dinkinesh spectra (filled circles—black is the close approach spectrum, and magenta is the departure spectrum) are shown to agree with LL and L chondrites.

measured band parameters of Dinkinesh suggest that it is mineralogically similar to LL/L chondrites, but it is not consistent with H chondrite spectra. LL/L chondrites have the highest olivine content among ordinary chondrite meteorite classes (e.g., H. Y. McSween et al. 1991), consistent with Dinkinesh’s location in the inner Main Asteroid belt (e.g., P. P. Vernazza et al. 2014; E. A. Cloutis et al. 2015)

Lastly, Dinkinesh’s $3.1\ \mu\text{m}$ band has an apparent depth of $\sim 6\%$ (Figure 7(c)). However, we note that LEISA was operating outside of its designed calibration range and temperature effects are nonlinear. We therefore urge caution in interpreting these longer wavelengths. We consider it likely that an absorption is present, but the accuracy of the depth and shape cannot be verified without other observations, including validation of any small thermal emission. Absorptions in this wavelength range are generally associated with hydration, so it may seem unexpected to see such an absorption on an S-complex asteroid. However, $3\ \mu\text{m}$ bands have been detected on a number of other nominally anhydrous bodies, including the Moon (e.g., C. Pieters et al. 2009; J. M. Sunshine et al. 2009), (4) Vesta (M. C. De Sanctis et al. 2012), NEAs (A. S. Rivkin et al. 2018; L. E. McGraw et al. 2022, 2024), L-type MBAs (J. J. Gomez Barrientos et al. 2024), and S-complex MBAs (M. M. McAdam et al. 2024). Hydration on these bodies has been attributed to interactions with the solar wind and/or physical contamination from impacts with more hydrated material. Furthermore, ordinary chondrite meteorite analogs (J. N. Grossman et al. 2000, R. H. Jones et al. 2014) and even samples returned from a similar L/LL-type ordinary-chondrite-like asteroid, Itokawa (Z. Jin & M. Bose 2019), show evidence of hydration among nominal anhydrous mineralogy.

Dinkinesh’s $3\ \mu\text{m}$ band appears deeper than the bands detected on several NEAs (some of which are similar size as Dinkinesh) and does not match any of the spectral shapes identified by L. E. McGraw et al. (2022). The Dinkinesh band also has no good matches among MBAs, being deeper than most of the $3\ \mu\text{m}$ bands detected on larger S-complex MBAs

(M. M. McAdam et al. 2024) but less deep than C-complex MBAs such as (24) Themis (A. Rivkin & J. Emery 2010; Figure 7(c)). We again point out, however, that the depth and shape of the observed band may not be accurate owing to the operating temperature issues described. While the details of the $3\ \mu\text{m}$ band are uncertain, it is important to note that the $3\ \mu\text{m}$ bands on Dinkinesh and Selam are indistinguishable from each other. This suggests that the hydration either is intimately integrated into the bulk composition of Dinkinesh, i.e., inherent, or accumulated, likely via space weathering, since Selam was formed, which, based on dynamic simulation, is estimated to be $\sim 1\text{--}10\ \text{Ma}$ (H. F. Levison et al. 2024; C. C. Merrill et al. 2024). We are unable to distinguish between possible sources of the band on Dinkinesh.

6. Conclusions

L’Ralph in-flight performance has been stable to date. MVIC has shown good in-flight radiometric stability, and its performance meets requirements in every channel with no major changes from ground calibration. LEISA’s flight thermal performance has been better than expected, allowing for earlier calibration campaigns than originally planned. The LEISA radiometric calibration and pixel size have been updated since ground calibration using scans of Arcturus. Applying the new calibration to Dinkinesh flyby data shows that the asteroid spectra are in reasonable agreement with those of other S- and Sq-type asteroids, with the presence of 1 and $2\ \mu\text{m}$ pyroxene bands. Dinkinesh is spectrally, and likely mineralogically, similar to LL/L-type ordinary chondrite meteorites. We also show evidence for a $3\ \mu\text{m}$ band, though calibration uncertainties limit its interpretation. Follow-up spectral observations (e.g., by James Webb Space Telescope) would be valuable for confirming and identifying the origin and significance of this band.











Calibration performance and trending work are ongoing and will include regular, brief, stellar, and solar calibrations. A larger, comprehensive calibration campaign is planned for when the spacecraft reaches 4 au and instruments reach their

full operating conditions, similar to those expected at the Trojans. These planned activities include a full radiometric calibration of L'Ralph using a range of standard stars. These future calibrations, as well as observations of the MBA (52246) Donaldjohanson in 2025 April, may also facilitate future recalibration of the Dinkinesh data.

Acknowledgments

The authors thank the entire L'Ralph support teams for their continued support of the instrument even after launch, particularly the thermal team that correctly predicted the LEISA operating temperatures. The Lucy mission is funded through the NASA Discovery Program by contract No. NNM16AA08C. All calibrated L'Ralph data can be retrieved from the PDS small bodies node at doi:10.26007/99kk-6s03 and doi:10.26007/f61e-0f52 (D. D. Reuter et al. 2024a; 2024b).

ORCID iDs

Amy A. Simon  <https://orcid.org/0000-0003-4641-6186>
 Hannah H. Kaplan  <https://orcid.org/0000-0002-6562-9462>
 William M. Grundy  <https://orcid.org/0000-0002-8296-6540>
 Richard P. Binzel  <https://orcid.org/0000-0002-9995-7341>
 Joshua Emery  <https://orcid.org/0000-0001-9265-9475>
 Jessica Sunshine  <https://orcid.org/0000-0002-9413-8785>
 Harold F. Levison  <https://orcid.org/0000-0001-5847-8099>
 Simone Marchi  <https://orcid.org/0000-0003-2548-3291>
 Keith S. Noll  <https://orcid.org/0000-0002-6013-9384>
 John Spencer  <https://orcid.org/0000-0003-4452-8109>

References

Binzel, R. P., DeMeo, F. E., Turtelboom, E. V., et al. 2019, *Icar*, **324**, 41
 Binzel, R. P., Rivkin, A. S., Bus, S. J., Sunshine, J. M., & Burbine, T. H. 2001, *M&PS*, **36**, 1167
 Binzel, R. P., Rivkin, A. S., Stuart, J. S., et al. 2004, *Icar*, **170**, 259
 Blank, R., Anglin, S., Beletic, J., et al. 2012, *Proc. SPIE*, **8453**, 845310
 Bohlin, R. C., Gordon, K. D., & Tremblay, P-E. 2014, *PASP*, **126**, 711
 Bolin, B. T., Noll, K. S., Caiazzo, I., Fremling, C., & Binzel, R. P. 2023, *Icar*, **400**, 115562
 Cloutis, E. A., Sanchez, J. A., Reddy, V., et al. 2015, *Icar*, **252**, 39
 De Sanctis, M. C., Combe, J. P., Ammannito, E., et al. 2012, *ApJL*, **758**, L36

Dunn, T. L., McCoy, T. J., Sunshine, J. M., & McSween, H. Y. 2010, *Icar*, **208**, 789
 Garrison, M., Reuter, D., Simon, A., et al. 2022, in 2022 IEEE Aerospace Conf. (AERO) (Piscataway, NJ: IEEE)
 Gomez Barrientos, J., de Kleer, K., Ehlmann, B. L., et al. 2024, *ApJL*, **967**, L11
 Grossman, J. N., Alexander, C. M., Wang, J., & Brearley, A. J. 2000, *M&PS*, **35**, 467
 Jones, R. H., McCubbin, F. M., Dreeland, L., et al. 2014, *GeoCoA*, **132**, 120
 Labsphere 2017, Technical Guide: Integrating Sphere Theory and Applications, <https://www.labsphere.com/wp-content/uploads/2021/09/Integrating-Sphere-Theory-and-Applications.pdf>
 Levison, H. F., Marchi, S., Noll, K. S., et al. 2024, *Natur*, **629**, 1015
 Levison, H. F., Olkin, C. B., Noll, K. S., et al. 2021, *PSJ*, **2**, 171
 Marsset, M., Vernazza, P., Broz, M., et al. 2024, *Natur*, **634**, 561
 McAdam, M. M., Thomas, C. A., McGraw, L., Rivkin, A. S., & Emery, J. P. 2024, *PSJ*, **5**, 254
 McGraw, L. E., Emery, J. P., Thomas, C. A., et al. 2022, *PSJ*, **3**, 243
 McGraw, L. E., Emery, J. P., Thomas, C. A., & Rivkin, A. R. 2024, *Icar*, **422**, 116252
 McSween, H. Y., Bennett, M. E., & Jarosewich, E. 1991, *Icar*, **90**, 107
 Merrill, C. C., Kubas, A. R., Meyer, A. J., & Raducan, S. D. 2024, *A&A*, **684**, L20
 Montanaro, M., Lunsford, A., Tesfaye, Z., Wenny, B., & Reuter, D. 2014, *RemS*, **6**, 8803
 Olkin, C. B., Levison, H. F., Vincent, M., et al. 2021, *PSJ*, **2**, 172
 Olkin, C. B., Vincent, M., Adam, C., et al. 2024, *SSRv*, **220**, 47
 Pearlman, A., Montanaro, M., Efremova, B., et al. 2020, *ITGRS*, **59**, 2715
 Pieters, C. M., Goswamy, J. N., Clark, R. N., et al. 2009, *Sci*, **326**, 568
 Polishook, D., DeMeo, F. E., Burt, B. J., et al. 2023, *PSJ*, **4**, 229
 Rayner, J. T., Cushing, M. C., & Vacca, W. D. 2009, *ApJS*, **185**, 289
 Reuter, D., Simon, A., Lunsford, A., et al. 2024a, Lucy L'Ralph LEISA Dinkinesh Calibrated Data Collection, urn:nasa:pds:lucy.leisa:data_dinkinesh_calibrated::1.0 NASA Planetary Data System, doi:10.26007/99kk-6s03
 Reuter, D., Simon, A., Lunsford, A., et al. 2024b, Lucy L'Ralph MVIC Dinkinesh Calibrated Data Collection, urn:nasa:pds:lucy.mvic:data_dinkinesh_calibrated::1.0, NASA Planetary Data System, doi:10.26007/f61e-0f52
 Reuter, D. C., Simon, A. A., Hair, J., et al. 2018, *SSRv*, **214**, 54
 Reuter, D. C., Simon, A. A., Lunsford, A., et al. 2023, *SSRv*, **219**, 69
 Reuter, D. C., Stern, S. A., Scherrer, J., et al. 2008, *SSRv*, **140**, 129
 Rivkin, A. S., & Emery, J. P. 2010, *Natur*, **464**, 1322
 Rivkin, A. S., Howell, E. S., Emery, J. P., & Sunshine, J. 2018, *Icar*, **304**, 74
 Simon, A. A., Reuter, D. C., Gorius, N., et al. 2018, *RemS*, **10**, 1486
 Simon, A. A., Reuter, D. C., & Laretta, D. S. 2021, *JATIS*, **7**, 020501
 Spencer, J. R., Bell, J. F., Christensen, P. R., et al. 2024, *SSRv*, **220**, 3
 Sunshine, J. M., Farnham, T. L., Feaga, L. M., et al. 2009, *Sci*, **326**, 565
 Vernazza, P., Zanda, B., Binzel, R. P., et al. 2014, *ApJ*, **791**, 120
 Zin, J., & Bose, M. 2019, *SciA*, **5**, eaav8106